

# GPR Phase-Based Techniques for Profiling Rough Surfaces and Detecting Small, Low-Contrast Landmines Under Flat Ground

Bin Sai, *Member, IEEE*, and Leo P. Ligthart, *Fellow, IEEE*

**Abstract**—In this paper, we present a new technique whereby phase variation signatures are used to profile two-dimensional (2-D) rough surfaces and to discern shallowly buried, small, low-contrast landmines under a flat ground. The method has been tested using data measured over a composite surface containing two rough dielectric surface patches, and over a flat ground under which small, low-contrast antipersonnel (AP) landmines are shallowly buried. The results show that the phase-based technique is capable of profiling rough surfaces and of detecting small, low-contrast landmines with different internal structures buried underneath a flat ground.

**Index Terms**—Ground penetrating radar, phase measurement, phase variation signatures, rough surfaces.

## I. INTRODUCTION

IT IS A VERY challenging task to design a reliable, easily interpretable and less time-consuming operational system for landmine detection that works well under various environmental conditions. Ground-penetrating radar (GPR) is recognized as a promising sensor for detecting buried landmines. In this case, the GPR antenna(s) must be elevated above the ground. This requirement results in heavy surface clutter, especially when the ground is rough [1], [2]. The different scenarios for detecting landmines can be categorized in terms of following three basic characteristics: 1) contrast (targets with low or high contrast); 2) surface profile (targets under a rough surface or flat surface); 3) depth (shallow or deep subsurface targets). The object contrast has a direct impact on the signal-to-clutter ratio. For a plastic landmine with a relative permittivity of 2.9 (TNT) and conductivity of  $8.7 \times 10^{-4}$  S/m at 3 GHz [3] buried under a flat dry sandy soil with a relative permittivity of 4 [3] and conductivity of  $4.1 \times 10^{-3}$  S/m [4], the signal-to-clutter ratio is below  $-10$  dB [5], and even much lower for a rough ground. The low contrast in electromagnetic properties of the buried objects and their surrounding soil means that signals from objects in the near-surface area can be corrupted or obscured by the ground surface clutter. On the other hand, signal echoes from deeply buried objects, or from shallowly buried but high-con-

trast objects, can be segregated from the surface clutter if the GPR system has a sufficient dynamic range and a high sensitivity [6]. In order to detect shallowly buried, small, low-contrast landmines, in general one needs to use higher frequencies in order to achieve a better resolution. Consequently, one has to deal with rough surfaces as well as possible soil attenuation for shorter wavelengths. Thus, it is one of the worst but most commonly encountered scenarios in actual minefields that small nonmetallic landmines are buried just beneath a rough ground surface [7]. The profiling of rough surfaces is, therefore, needed for the removal of rough surface scattering effects [8], a task particularly crucial for detecting and imaging shallow, low-contrast subsurface objects with sizes of a few centimeters, such as antipersonnel (AP) landmines.

Various available analyses and numerical simulations have shown the considerable complexity of two-dimensional (2-D) and/or three-dimensional (3-D) rough surface scattering [9]–[15]. Recent studies on scattering from an object buried under a rough surface have been carried out with statistical modeling in the frequency and time domains [16]–[22]. In particular, the scattering from a dielectric target buried near a clutter object underneath 2-D rough surfaces (3-D scattering problem) has been investigated statistically [23]. The results show that the total scattered field is dominated by the rough surfaces; the average scattered field from the buried target accounts for around 6% of the total scattered field. This suggests that one cannot detect very shallowly buried, low-contrast targets without removing the effects of the rough surfaces. In this paper, we report on studies we have carried out for profiling rough surfaces and discerning small, low-contrast mine-like objects buried just beneath the flat surface. The underlying method is based on phase variation signatures extracted from data measured by a stepped-frequency continuous-wave (SFCW) GPR. The rest of this paper is organized as follows. The proposed methodology is described in Section II. The GPR measurement system configuration is given in Section III. The processing algorithms are described in Section IV. The experimental results for algorithm validation are discussed in Section V. Finally conclusions are given in Section VI.

## II. METHODOLOGY

In the standoff SFCW GPR system depicted in Fig. 1, the generated signal is radiated by the transmit antenna toward a target area on the ground. Part of the signal is scattered at the ground surface, while the rest penetrates into the ground. The signal

Manuscript received September 26, 2002; revised April 23, 2003. This work was supported by the Netherlands Technology Foundation (STW), the applied science division of NWO.

B. Sai is with Enraf B.V. of Delft Instruments Group, 2628 XJ Delft, The Netherlands.

L. P. Ligthart is with the International Research Centre for Telecommunications-Transmission and Radar, Faculty of Electrical Engineering, Delft University of Technology, 2628 CD Delft, The Netherlands.

Digital Object Identifier 10.1109/TGRS.2003.817204

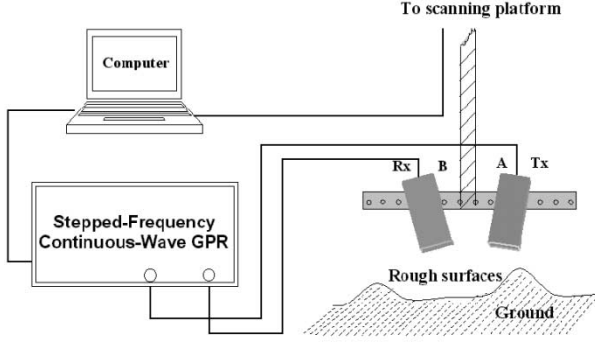


Fig. 1. Schematic diagram of the GPR measurement system setup: antenna “A” is tilted  $1^\circ$  to the left, while antenna “B” is angled  $4^\circ$  to the right.

(wave) travels a certain distance in the ground until it impinges on the target (anomaly). As a result, part of the wave is scattered and passes through the ground–air interface toward the receive antenna. The whole process is illustrated in Fig. 2, where  $S_{\text{Syn}}(\omega_i)$  is the output signal from the frequency synthesizer at the angular frequency  $\omega_i$ ;  $H_{\text{tl}}(\omega_i)$  represents the transfer function of the transmission channel;  $H_{\text{ta}}(\omega_i)$  is the transmitting-antenna transfer function;  $H_{\text{pt}}(\omega_i)$  is the wave propagation factor starting from the antenna phase center to the ground surface;  $H_{\text{a-g}}(\omega_i)$  is the transfer function of the air–ground interface;  $H_{\text{gr}}(\omega_i)$  denotes the soil transfer function for the distance between the ground surface and the depth to which the wave travels until it impinges on the target;  $H_{\text{tg}}(\omega_i)$  denotes the target echo transfer function;  $H_{\text{g-a}}(\omega_i)$  denotes the transfer function of the ground–air interface;  $H_{\text{pr}}(\omega_i)$  is the propagation factor starting from the ground–air interface toward the receiving-antenna phase center;  $H_{\text{ra}}(\omega_i)$  is the receiving-antenna transfer function;  $H_{\text{rc}}(\omega_i)$  represents the transfer function of the reception channel;  $S_{\text{out}}(\omega_i)$  is the output of the receiver channel. The signal samples from in-phase ( $I$ ) and quadrature ( $Q$ ) channels can be combined to form a complex polar sample, which is particularly convenient for the analytical analysis. For an arbitrary antenna spatial sampling position, the signal relationship can be quantitatively described by

$$S_{\text{out}}(\omega_i) = S_{\text{Syn}}(\omega_i) \cdot H_{\text{tl}}(\omega_i) \cdot H_{\text{ta}}(\omega_i) \cdot H_{\text{pt}}(\omega_i) \cdot H_{\text{a-g}}(\omega_i) \cdot H_{\text{gr}}(\omega_i) \cdot H_{\text{tg}}(\omega_i) \cdot H_{\text{g-a}}(\omega_i) \cdot H_{\text{pr}}(\omega_i) \cdot H_{\text{ra}}(\omega_i) \cdot H_{\text{rc}}(\omega_i). \quad (1)$$

In the block diagram, the blocks indicated by w1, w2, and w3 can be characterized by means of the closed-loop internal calibration, antenna calibration, and external geometrical calibration, respectively. After the calibrations are performed for the blocks w1 and w2, (1) can be rewritten as

$$S'_{\text{out}}(\omega_i) = b \cdot H_{\text{pt}}(\omega_i) \cdot H_{\text{a-g}}(\omega_i) \cdot H_{\text{gr}}(\omega_i) \cdot H_{\text{tg}}(\omega_i) \cdot H_{\text{g-a}}(\omega_i) \cdot H_{\text{pr}}(\omega_i) \quad (2)$$

where  $S'_{\text{out}}(f_i)$  are the preprocessed signal data after the two calibrations have been accomplished, and  $b$  is a constant. We define the two-way propagation factor in air as

$$W = b \cdot H_{\text{pt}} \cdot H_{\text{pr}}. \quad (3)$$

We have then

$$\begin{aligned} S'_{\text{out}}(\omega_i) &= W \cdot H_{\text{a-g}}(\omega_i) \cdot H_{\text{gr}}(\omega_i) \cdot H_{\text{tg}}(\omega_i) \\ &\quad \cdot H_{\text{g-a}}(\omega_i) \cdot H_{\text{pr}}(\omega_i) \\ &= |W| \cdot |H_{\text{a-g}}(\omega_i)| \cdot |H_{\text{gr}}(\omega_i)|^2 \\ &\quad \cdot |H_{\text{tg}}(\omega_i)| \cdot |H_{\text{g-a}}(\omega_i)| \\ &\quad \cdot \exp[j(\varphi_w + \varphi_{\text{a-g}} + 2\varphi_{\text{gr}} + \varphi_{\text{tg}} + \varphi_{\text{g-a}})] \quad (4) \end{aligned}$$

where the phase of  $W$  contains the information about the surface-height variations due to the presence of rough surfaces. The external geometrical calibration for the block w3 is used to determine the factor  $W$  with respect to the reference plane. It can be seen in (4) that the preprocessed data are associated with the characteristics of the rough surface, air–soil interface, the target, and its surrounding soil.

#### A. Calibration Procedures for Phase Processing

For the coherent SFCW GPR system, the system calibration is carried out by its specified internal calibration procedures, which exclude the antennas and measurement geometry. As the GPR operates in close proximity to the ground, the local soil, and near-range objects can severely affect the free-space phase characteristics of the GPR antennas. We can take advantage of these influences to explore the characteristics of the near-range scattering objects. Accordingly, the free-space near-range phase characteristics of the GPR antennas should be measured over the operational frequency range. The measurement geometry can be calibrated with respect to a predefined reference plane. For example, one may choose a flat portion of the air–ground interface and place a metal plate on it. At each frequency, one can obtain the phase variation associated with the distance from the phase center of the transmit antenna to the reflection point on the reference plane and back to the phase center of the receive antenna. The measured phase variations can be used to calibrate out the measurement geometry.

#### B. Profiling Rough Surfaces From Measured Data

To profile the rough interface between air and a homogeneous soil,<sup>1</sup> the phase variations extracted from the data acquired by a SFCW GPR were used as a measure of the difference in the propagation paths between the antenna phase center and the phase center of a rough-surface scattering point. The difference in the propagation paths contains the surface height information. The variations of the phase difference can be processed at every spatial sampling position in order to deduce the surface height distribution by means of geometrical optics. In this way, the image of the rough surface can be constructed.

#### C. Subsurface Object Phase Signatures

It can be seen from (4) that the phase contains useful information about physical and geometrical properties of the buried objects. We can use the phase data measured over the different objects buried under a flat ground to explore the properties or property changes of different scattering objects, in particular the

<sup>1</sup>The scattering from small, low-contrast landmines shallowly buried under rough surfaces has little impact on the 3-D rough surface scattering that dominates the scattering mechanisms near the surface area.

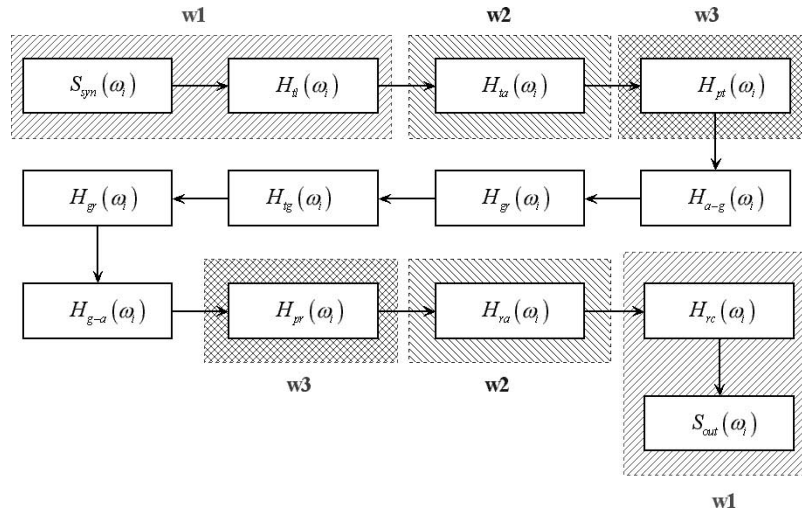


Fig. 2. Block diagram of the input–output relationship for a standoff GPR system.

internal structure of the objects [24]. The object phase signatures can reflect the inhomogeneities embedded in a homogeneous background medium. They are associated with the subsurface object's discernible depth, the difference in electromagnetic properties, as well as the internal structures between the object and its ambient medium.

### III. GPR MEASUREMENT SYSTEM

#### A. SFCW Waveform

The SFCW GPR system generates and emits a number of continuous-wave (CW) frequency tones, covering a wide frequency range [25]. Its waveform can be expressed as a frequency-stepped pulse train, *viz.*,

$$x(t) = \sum_{i=0}^N A_i \cos [2\pi (f_L + i\Delta f)t + \theta_i] \text{rect} \left[ \frac{t - iT - \frac{T}{2}}{T} \right] \quad (5)$$

where  $N$  is the number of frequency steps,  $f_L$  is the starting frequency,  $\Delta f$  is the frequency interval,  $\text{rect}[\cdot]$  denotes a rectangular pulse function with pulse repetition interval of  $T$ ,  $\theta_i$  is the initial phase at  $t = 0$ , and  $A_i$  is the amplitude of the frequency tone of  $f_L + i\Delta f$ . The frequency interval is determined on the basis of the Nyquist sampling criterion for unambiguously sampling a complex signal [26], specifically,  $\Delta f \leq v_p/2l$ , where  $l$  is the target range extent and  $v_p$  is the propagation velocity in the medium. Fig. 3 shows the spectrum of a simulated SFCW waveform consisting of 16 frequencies. The complex data, formed by sampling the downconverted baseband signal for a target located at a distance  $r_1$  from a monostatic antenna at a spatial sampling position, are expressed as

$$C[i] = A_i |W| |H_{tg}(f_L + i\Delta f)| \cdot \exp \left[ -j \frac{4\pi r_1}{v_p} (f_L + i\Delta f) + \varphi_{tg}(f_L + i\Delta f) \right]. \quad (6)$$

These data contain the target phase signature at the frequency  $f_L + i\Delta f$ . The synthetic range profile can be obtained by performing an inverse discrete Fourier transform of the complex

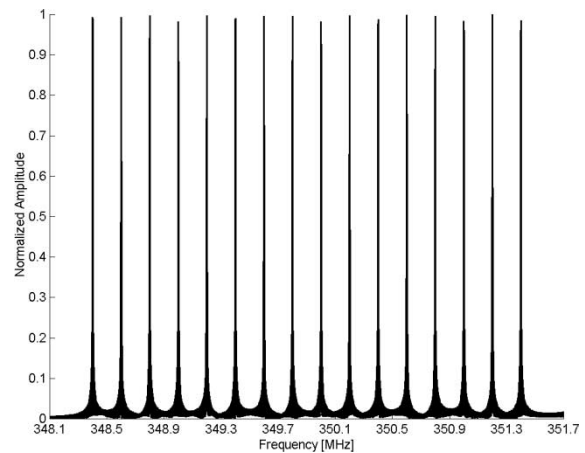


Fig. 3. Spectrum of simulated SFCW waveform consisting of 16 frequencies.

data array [25]. By its nature, the SFCW waveform produces a high range-sidelobe level on the synthesized range profile. Consequently, one has to use weighting functions in order to reduce the sidelobe level at the cost of the range resolution [27].

#### B. Open-Ended Waveguide Antennas for SFCW GPR

Because of the tradeoff between the down-range resolution and penetration depth in the ground, the wideband waveform with low-frequency content is preferred in most GPR systems [28]–[30]. Accordingly, broadband, low-gain and wide-beam antennas are commonly adopted, except for a few distinctive parabolic GPR antenna systems [31], [32]. In the setup of our SFCW GPR system, as shown in Fig. 1, two conventional wide-beam open-ended rectangular waveguide (OERW) antennas were adopted in a fixed-offset copolarized (horizontal polarization) configuration. The antennas were used over an ultrawide-frequency band ranging from 2.3–4.3 GHz. At the central frequency, the measured 3-dB beam widths of the antenna are  $60^\circ$  in the H-plane, and  $95^\circ$  in the E-plane. The dispersion effects of the antennas can be observed in Fig. 4(a), where the phase responses of the two *vis-à-vis* antennas are converted to the propagating time taken through these two

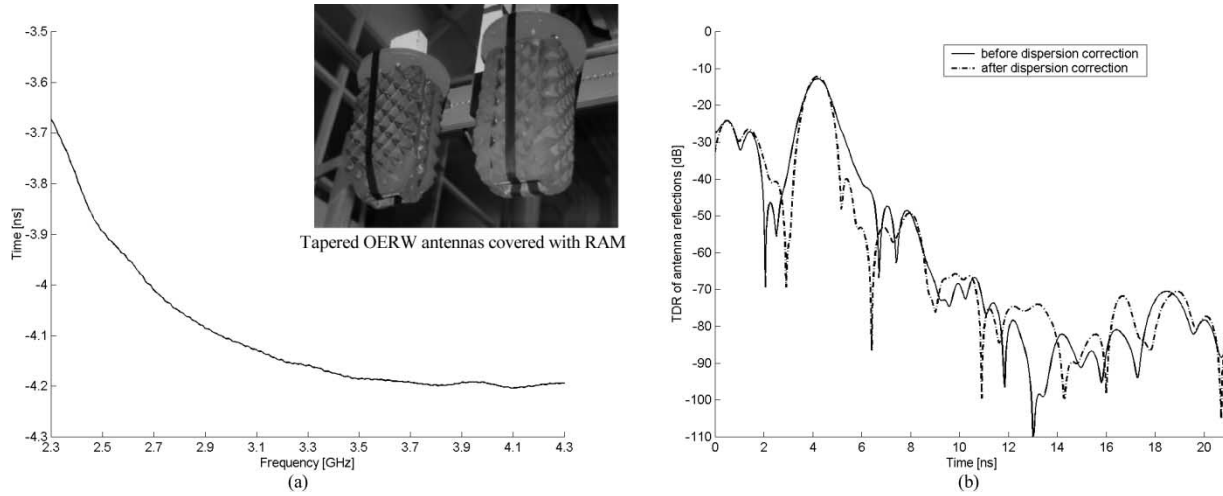


Fig. 4. Dispersion effects of the OERW antennas. (a) Propagation time through the two *vis-à-vis* OERW antennas. (b) Comparison before and after antenna dispersion correction.

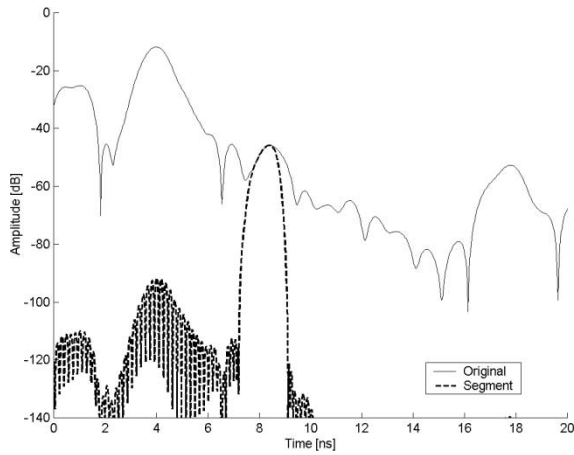


Fig. 5. Sliced segment of the synthetic range profile from 7.9–8.4 ns.

antennas. The results in Fig. 4(b) give a comparison before and after correction of the OERW antenna dispersion [33].

#### IV. PROCESSING ALGORITHMS

##### A. Profiling Dielectric Rough Surfaces

In order to extract the phase variations associated with rough surfaces from the measured data, the synthetic range profile was sliced into segments by means of a coherent high-resolution gating technique (cf. Fig. 5), which is similar to that used in the time-domain measurements [34], [35]. The selection of the size of the segments depends on the gating limit and the measurement geometry. The phase responses in each segment were retrieved by means of a discrete Fourier transform of the gated complex range profile. In this way, the phase variations related to the surface height variations can be treated in a piecewise range segment. From (4) the preprocessed phase data measured over the rough interface between air and a homogeneous soil can be expressed as

$$\psi^m(f_i) = \varphi_w^m(f_i) + \varphi_{agr}^m(f_i) \quad (7)$$

where  $m$  is the antenna spatial sampling position index and  $\varphi_{agr}$  denotes the phase of the reflected/scattered signal due to the change in electromagnetic properties on the air–soil interface. It is known that the phase data acquired from  $I$  and  $Q$  components are not the true phase values but the ones wrapped into the principal-value interval  $[-\pi, \pi]$  by means of the following nonlinear mathematical operation:

$$\psi = 2\pi k + \phi. \quad (8)$$

Here,  $k$  is an integer ensuring that  $\psi \in [-\pi, \pi]$ ,  $\phi$  represents the true phase value. A phase unwrapping is needed in order to eliminate the phase ambiguity and, hence, the height ambiguity. According to (7), the true phase value for two-way propagation from the monostatic antenna<sup>2</sup> phase center to the rough-surface scattering point  $P$  at  $(x_p, y_p, z_p)$  can be expressed as

$$\phi_p^m(f_i) = \frac{4\pi r_{mp}}{c} f_i + \varphi_p^m(f_i) \quad (9)$$

where  $r_{mp}$  is the distance between the phase center of the antenna at the spatial sampling position  $m$  to the rough-surface scattering point  $P$ ,  $c$  is the speed of light in air, and  $\varphi_p^m(f_i)$  denotes the phase of the reflected/scattered signal due to the change in electromagnetic properties on the air–soil interface at frequency  $f_i$ . Thus, at two nearby frequencies, the difference of the true phase data scattered from the same scattering point  $P$  can be written as

$$\Delta\phi_p^m(f_i, f_j) = \frac{4\pi r_{mp}}{c} \Delta f_{ij} + \Delta\varphi_p^m(f_i, f_j) \quad (10)$$

where  $\Delta\phi_p^m(f_i, f_j) = \phi_p^m(f_i) - \phi_p^m(f_j)$ ,  $\Delta\varphi_p^m(f_i, f_j) = \varphi_p^m(f_i) - \varphi_p^m(f_j)$ , and  $\Delta f_{ij} = f_i - f_j$ . If  $\Delta f_{ij}$  can be chosen in such a way that the unambiguous range is larger than the one-way propagation range and if the electromagnetic properties of the soil at two nearby frequencies have negligible changes, then the integer value  $k$  in (8) will remain unchanged

<sup>2</sup>For the sake of simplicity, we adopt here a monostatic antenna configuration. However, the approach is also applied to a bistatic configuration, as shown in the results given in Section V.

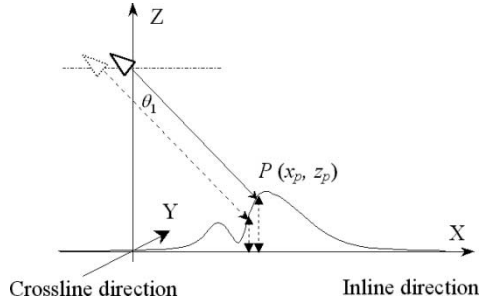


Fig. 6. Vertical plane ( $y = 0$ ) of general monostatic measurement geometry where a reference plane is located at  $z = 0$ .

with respect to these two frequencies. Therefore, we can state that if

$$\Delta f_{ij} \leq \frac{c}{2r_{\max}} \quad (11)$$

$$\varepsilon_i = \varepsilon_j; \mu_i = \mu_j, \quad (12)$$

then

$$\Delta \phi_p^m(f_i, f_j) = \Delta \psi_p^m(f_i, f_j) \quad (13)$$

$$\Delta \varphi_p^m(f_i, f_j) = 0. \quad (14)$$

Here,  $r_{\max}$  denotes the maximal of the one-way propagation range in a monostatic configuration, or the maximal of either propagation range in a bistatic configuration;  $\varepsilon_i$  and  $\varepsilon_j$ ,  $\mu_i$  and  $\mu_j$  denote the effective permittivity and permeability of the surface layer of the soil at the frequencies  $f_i$  and  $f_j$ , respectively;  $\Delta \psi_p^m(f_i, f_j)$  denotes difference of the wrapped phase data at the two frequencies;  $\Delta f_{ij}$  is referred to as the unambiguous frequency interval (UFI). Hence, by combining (10), (13), and (14), we can derive the one-way propagation range,  $r_{\text{mp}}$  from the wrapped phase data at two frequencies within the maximum UFI

$$r_{\text{mp}} = c \frac{\Delta \psi_p^m(f_i, f_j)}{4\pi \Delta f_{ij}}. \quad (15)$$

For a given measurement geometry, the external calibration for the block w3 in Fig. 2 determines the one-way propagation distance  $r_{\text{cr}}$  from the antenna phase center to the reference plane (a metal plate); the latter is expressed as

$$r_{\text{cr}} = c \frac{\Delta \psi_{\text{cr}}(f_i, f_j)}{4\pi \Delta f_{ij}} \quad (16)$$

where  $\psi_{\text{cr}}$  is the difference of the wrapped phase data with respect to the metal plate for two frequencies. Fig. 6 illustrates a general geometry for the monostatic measurement of the rough surface, in which the height of a rough-surface scattering point  $P$  at  $(x_p, y_p, z_p)$  relative to the reference plane ( $z = 0$ ) can be expressed in general notation by combining (15) and (16)

$$h_p^{m,n} = c \frac{\Delta \psi_{\text{cr}} - \Delta \psi_p^{m,n}}{4\pi \Delta f_{ij}} \cos \theta_1. \quad (17)$$

In this expression,  $\theta_1$  is the antenna boresight look angle off-nadir,  $m$  and  $n$  are integers corresponding to the inline and crossline number indexes used in the 2-D grid scan. The antenna spatial sampling positions on the 2-D scanning grid can be

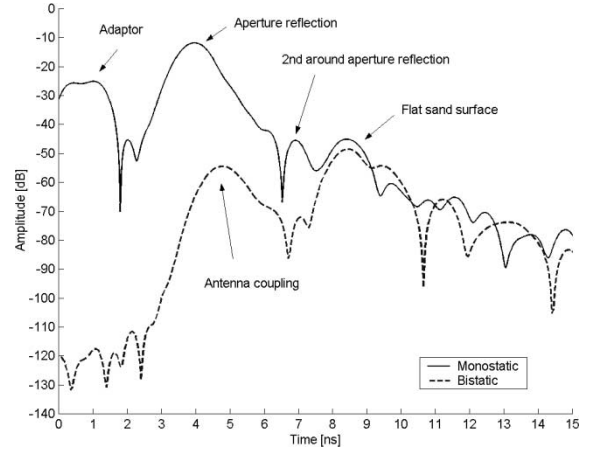


Fig. 7. Time-domain response of OERW antennas 68 cm above the sand surface.

mapped to the corresponding points of the surface area. Therefore, we can rewrite (17) in a more general form by omitting the subscript  $p$  as

$$Z_{x,y} = c \frac{\Delta \psi_{\text{cr}} - \Delta \psi_{x,y}}{4\pi \Delta f_{ij}} \cos \theta_1 \quad (18)$$

where  $z_{x,y}$  is the surface height distribution relative to the reference surface ( $z = 0$ ), and  $x$  and  $y$  denote the inline and crossline coordinates for the surface area.

### B. Detection of Small Low-Contrast Objects Under Flat Ground

From (4), at the frequency  $f_i$ , the difference of the phase measured from two adjacent closely spaced spatial-sampling positions with respect to an object buried beneath the flat homogeneous soil can be expressed as

$$\psi^m(f_i) = \varphi_{\text{const}}(f_i) + 2\varphi_{\text{gr}}^m(f_i) + \varphi_{\text{tg}}^m(f_i) \quad (19)$$

and

$$\psi^{m+1}(f_i) = \varphi_{\text{const}}(f_i) + 2\varphi_{\text{gr}}^{m+1}(f_i) + \varphi_{\text{tg}}^{m+1}(f_i) \quad (20)$$

where  $m$  is the index number of the inline spatial-sampling positions,  $\varphi_{\text{const}} = \varphi_{\text{a-g}}^m + \varphi_{\text{g-a}}^m + \varphi_w^m$  is a constant,  $\varphi_{\text{gr}}$  is the phase of the soil transfer function for the distance between the ground and the depth to which the wave travels until it impinges on the object, and  $\varphi_{\text{tg}}$  represents the phase of the target echo transfer function. We found that the internal structures of the penetrable objects can perturb the phase property of a continuous wave and cause the phase variation. This allows one to distinguish objects with different internal structures located in the same homogeneous layer of soil [36].

## V. RESULTS AND DISCUSSION

The measurements using the SFCW ground-penetrating radar were carried out at an indoor wooden box (2.44 m long, 2.44 m wide, 1.2 m high), filled with completely dried and sieved sand to the height level of 0.8 m. The separation and elevation of the two OERW antennas were 27 and 68 cm, respectively. The range profile synthesized from the measured monostatic and bistatic data over the sandbox are given in Fig. 7.

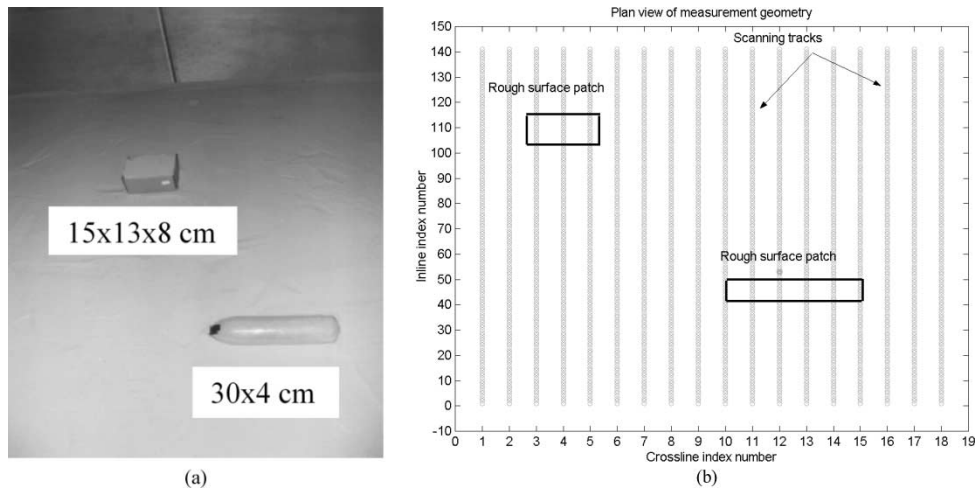


Fig. 8. Composite sandy surface comprising two rough surface patches. (a) Photograph of the actual composite surface. (b) Plan of measurement geometry (scanned area).

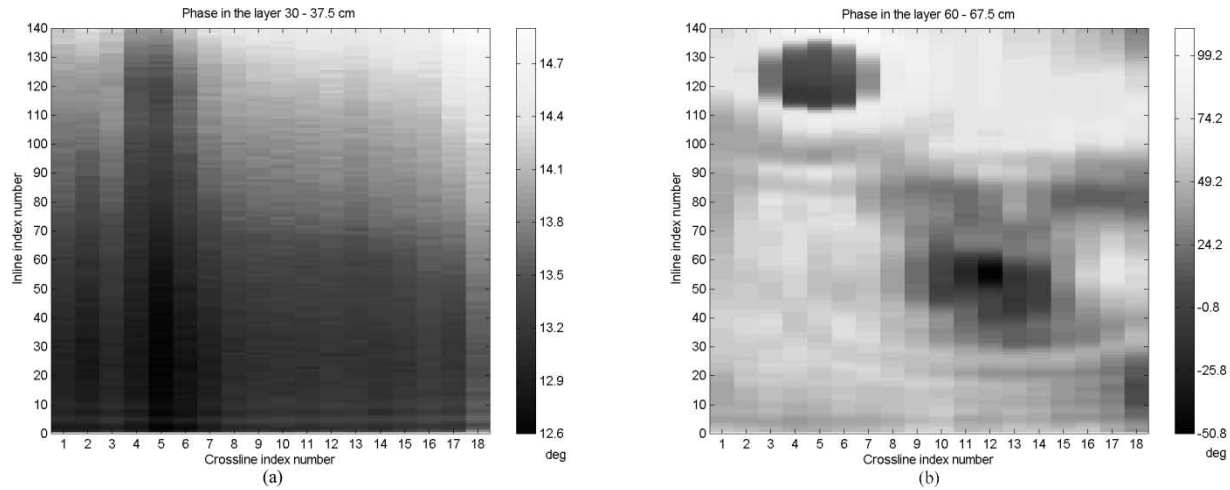


Fig. 9. Monostatic phase variations at 2.8 GHz, inline positions (cm) = inline index number  $\times$  1 cm; crossline positions (cm) = crossline index number  $\times$  5 cm. (a) For the layer of 30–37.5 cm. (b). For the layer of 60–67.5 cm.

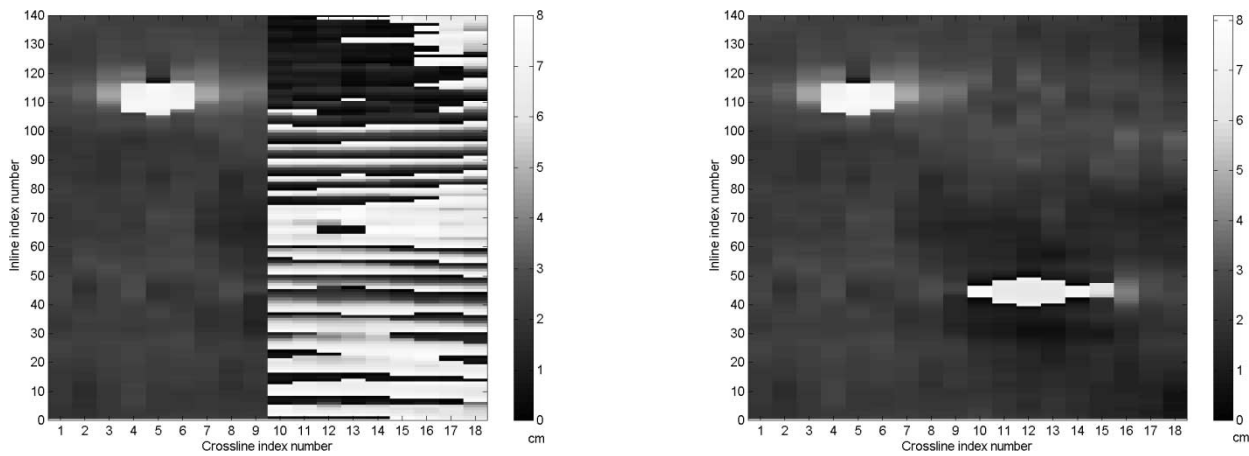


Fig. 10. Comparison of surface-height distribution with/without correction of height ambiguity.

Fig. 11. Reconstructed surface-height distribution of the composite surface: inline positions (cm) = inline index number  $\times$  1 cm; crossline positions (cm) = crossline index number  $\times$  5 cm.

*A. Measurement of Dielectric Rough Surface Patches*

We constructed a composite sandy surface containing two rough surface patches: a surface-laid sandy cube (15 cm long, 13 cm wide, and 8 cm high), and a horizontally half-buried

sandy cylinder, 30 cm long and 8.5 cm in diameter [Fig. 8(a)] The surface height is 8 cm for the sandy cube, and 0–4 cm variable for the sandy cylinder. The lateral separation between the two patches is 20 cm along the crossline direction and 58 cm

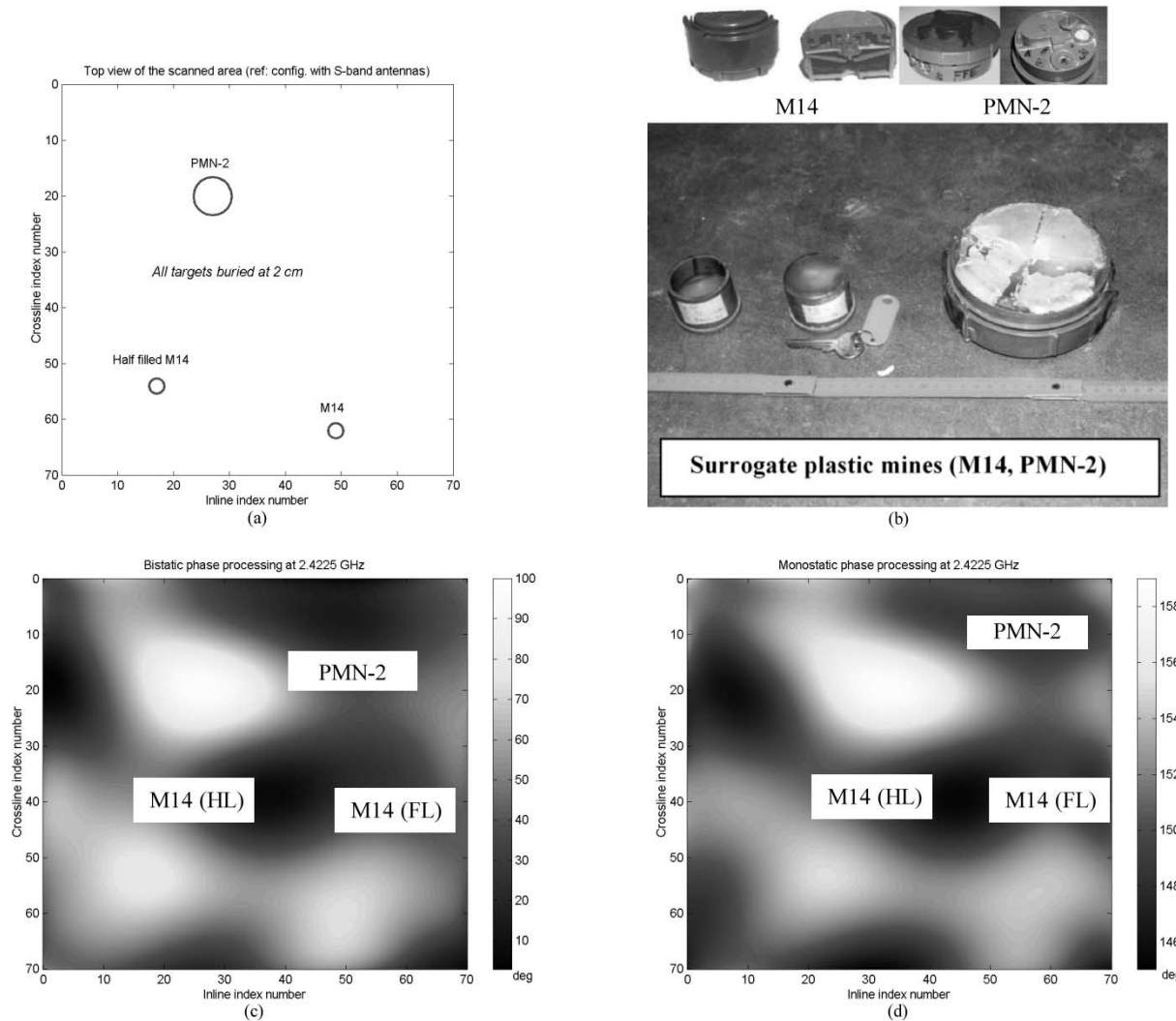


Fig. 12. Phase-based detection of three AP mines, one PMN2 with fully load, one M14 with half load (HL), and one M14 with full load (FL). Inline positions (cm) = inline index number  $\times$  2 cm; crossline positions (cm) = crossline index number  $\times$  2 cm. (a) Top view of the scanned area. (b) Photograph of three surrogate AP mines (opened for view). (Upper part) The picture of the real mines. (c) Bistatic phase-based detection result. (d) Monostatic phase-based detection result.

along the inline direction, respectively [see Fig. 8(b)]. The interval between two adjacent GPR spatial-sampling positions is 1 cm in the inline direction and 5 cm in the crossline direction, respectively. As an example, we selected a segment size of 7.5 cm and a frequency interval of 50 MHz. We obtained the phase variations with respect to 781 frequencies from 2.3–4.25 GHz. We simply chose a frequency of 2.8 GHz for analysis purposes. The 2.8-GHz monochromatic phase variations are shown in Fig. 9(a), indicating no scattering objects observed in the range segment of 30–37.5 cm. But, in the segment of 60–67.5 cm shown in Fig. 9(b), two scattering objects appear into the image. The linear color scale corresponds to phase variations in degrees. Because the footprint of the elevated OERW antennas (0.7 m on the sand surface on 3-dB level) is much larger than the lateral size of the rough surface patches, the images of the rough surfaces are defocused, particularly for the curved sandy cylinder. To improve the result, we coherently superposed the multiview phase data along the inline scan for all frequencies [37]. However, the superposition of different frequency components leads to a phase wrapping effect, resulting in a

surface height ambiguity that must be corrected [38]. The result in Fig. 10 shows a comparison between processing with and without unwrapping of ambiguous height. The linear color scale corresponds to the surface-height variations in centimeters. The reconstructed and actual rough surface patches are compared in Fig. 11. We see that there is good agreement between the reconstructed and the real ones.

#### B. Measurement of Small Plastic Landmines Shallowly Buried Under Flat Soil

We used three surrogate plastic AP landmines to test the phase-based detection algorithm. One is PMN-2 mine ( $\phi = 12.5$  cm,  $h = 5.2$  cm), and the other two are M14 mines ( $\phi = 5$  cm,  $h = 4.2$  cm). The three mines were physically buried at the same depth of 2 cm beneath the flat surface of dry sand in a triangular arrangement, as illustrated in Fig. 12(a). The PMN-2 and one of the M14 mines were fully loaded with wax ( $\epsilon_r = 2.4 - j0.03$  at 3 GHz) [3]. In order to examine the phase perturbation caused by the internal structure of a buried object, the other M14 mine was filled with wax and air, one

half each, as shown in Fig. 12(b). The interval between two adjacent GPR spatial-sampling positions is 2 cm in both inline and crossline directions. The results in Fig. 12(c) and (d) show that all three landmines are detectable by means of a bistatic and monostatic phase-based detection algorithm at a single frequency of 2.4225 GHz. The color scale corresponds to phase value in degrees. It is noted that the fully and half loaded M14 mines are detected by different phase values. The phase value of the fully loaded M14 is closer to the value of the background media, while the value of the half loaded M14 appears nearer to that of the PMN-2 mine. The phase distinction between the two M14 mines results from the difference in their internal structures. The degree of phase perturbation depends on the degree to which the internal structure of the object differs from that of its ambient medium. Since the real landmines are not fully loaded with explosives [7], the air gap inside landmines could be used as a feature to distinguish between landmines and some clutter objects, such as rocks and tree roots.

## VI. CONCLUSION

A phase-based technique for profiling dielectric rough surface patches and detecting small and low-contrast AP mines buried beneath the flat ground has been described. The technique exploited the phase variations induced by 3-D rough surface scattering to obtain the rough surface profile. With this technique, the rough surfaces reconstructed from the measured GPR data show good agreement with the actual ones. Moreover, we examined the phase perturbation caused by inhomogeneities of the internal structure of the penetrable objects in a sliced homogeneous soil layer. The results show that both fully and half loaded plastic M14 mines buried under the flat ground are detectable by means of a phase-based detection algorithm. However, the phase-based detection method is not suitable for a direct detection of landmines buried underneath a rough ground.

## REFERENCES

- [1] L. Carin, J. Sichina, and J. F. Harvey, "Microwave underground propagation and detection," *IEEE Trans. Microwave Theory Tech.*, vol. 50, pp. 945–952, Mar. 2002.
- [2] M. El-Shenawee, C. Rappaport, E. L. Miller, and M. B. Silevitch, "Three-dimensional subsurface analysis of electromagnetic scattering from penetrable/PEC objects buried under rough surfaces: Use of the steepest descent fast multipole method," *IEEE Trans. Geosci. Remote Sensing*, vol. 39, pp. 1174–1182, June 2001.
- [3] A. R. Von Hippel, Ed., *Dielectric Materials and Applications*. New York: Wiley, 1953.
- [4] J. E. Hipp, "Soil electromagnetic parameters as functions of frequency, soil density, and soil moisture," *Proc. IEEE*, vol. 62, pp. 98–103, Jan. 1974.
- [5] B. Sai, I. Morrow, and P. van Genderen, "Limits of detection of buried landmines based on local echo contrasts," in *Proc. 28th Eur. Microwave Conf. (EuMc), Workshop*, Amsterdam, The Netherlands, Oct. 1998, pp. 121–125.
- [6] B. Sai and P. van Genderen, "On the design of UWB GPR front-end for landmine detection," in *Proc. 5th Int. Radar Conf.*, Brest, France, May 1999.
- [7] DoD, *Mine Facts, Version 1.0*. Washington, DC: U.S. Dept. Defense, 1995.
- [8] V. Galdi, H. Feng, D. A. Castanon, and W. C. Karl, "Multifrequency subsurface sensing in the presence of a moderately rough air–soil interface via quasiray Gaussian beams," *Radio Sci.*, vol. 38, pp. 8–1/12, Dec. 2002.
- [9] P. Beckmann and A. Spizzichino, *The Scattering of Electromagnetic Waves from Rough Surfaces*. Norwood, MA: Artech House, 1987.
- [10] A. G. Voronovich, *Wave Scattering from Rough Surfaces*, 2nd ed. Berlin, Germany: Springer-Verlag, 1998.
- [11] S. M. Rao, D. R. Wilton, and A. W. Glisson, "Electromagnetic scattering from subsurface of arbitrary shape," *IEEE Trans. Antennas Propagat.*, vol. AP-30, pp. 409–418, May 1982.
- [12] K. A. Michalski and D. Zheng, "Electromagnetic scattering and radiation by subsurfaces of arbitrary shape in layered media: Parts I and II," *IEEE Trans. Antennas Propagat.*, vol. 38, pp. 335–352, Mar. 1990.
- [13] M. F. Chen and S. Y. Bai, "Computer simulation of wave scattering from a dielectric random rough surface in two dimensions—Cylindrical case," *J. Electromagn. Waves Appl.*, vol. 4, no. 10, pp. 919–1026, Oct. 1990.
- [14] A. K. Fung, S. Tjuatja, and C. Terré, "Numerical simulation of omnidirectional scattering from three-dimensional randomly rough dielectric surfaces," in *Proc. IGARSS*, vol. 1, Aug. 1994, pp. 261–263.
- [15] F. D. Hastings, J. B. Schneider, and S. L. Broschat, "A Monte-Carlo FDTD technique for rough surface scattering," *IEEE Trans. Antennas Propagat.*, vol. 43, pp. 1183–1191, Nov. 1995.
- [16] K. O'Neill, R. F. Lussky, Jr., and K. D. Paulsen, "Scattering from a metallic object embedded near the randomly rough surface of a lossy dielectric," *IEEE Trans. Geosci. Remote Sensing*, vol. 34, pp. 367–376, Mar. 1996.
- [17] M. El-Shenawee, "The multiple interaction model for nonshallow scatterers buried beneath 2-D random rough surfaces," *IEEE Trans. Geosci. Remote Sensing*, vol. 40, pp. 982–987, Apr. 2002.
- [18] V. Galdi, D. A. Castanon, and L. B. Felsen, "Multifrequency reconstruction of moderately rough interfaces via quasiray Gaussian beams," *IEEE Trans. Geosci. Remote Sensing*, vol. 40, pp. 453–460, Feb. 2002.
- [19] G. F. Zhang, L. Tsang, and K. Pak, "Studies of the correlation function of scattering by random rough surfaces with and without a buried object," *IEEE Trans. Geosci. Remote Sensing*, vol. 35, pp. 444–453, Mar. 1997.
- [20] T. J. Cui and W. C. Chew, "Fast algorithm for electromagnetic scattering by buried 3-D dielectric objects of large size," *IEEE Trans. Geosci. Remote Sensing*, vol. 37, pp. 2597–2608, Sept. 1999.
- [21] T. Dogaru and L. Carin, "Time-domain sensing of targets buried under a Gaussian, exponential, or fractal rough interface," *IEEE Trans. Geosci. Remote Sensing*, vol. 39, pp. 1807–1819, Aug. 2001.
- [22] A. v. d. Merwe and I. J. Gupta, "A novel signal processing technique for clutter reduction in GPR measurements of small, shallow landmines," *IEEE Geosci. Remote Sensing*, vol. 38, pp. 2627–2637, Nov. 2000.
- [23] M. El-Shenawee and C. M. Rappaport, "Monte Carlo simulations for clutter statistics in minefields: AP-mine-like-target buried near a dielectric object beneath 2-D random rough ground surfaces," *IEEE Trans. Geosci. Remote Sensing*, vol. 40, pp. 1416–1426, June 2002.
- [24] B. Sai and L. P. Ligthart, "Detection and imaging of small buried 3-D nonmetallic objects with multistatic phase-based GPR signatures," in *Proc. IGARSS*, vol. 4, July 2002, pp. 1988–1990.
- [25] K. Lizuka and A. P. Freundorfer, "Step-frequency radar," *J. Appl. Phys.*, vol. 56, no. 9, pp. 2572–2583, Nov. 1984.
- [26] D. R. Wehner, *High-Resolution Radar*, 2nd ed. Norwood, MA: Artech House, 1995.
- [27] F. J. Harris, "On the use of windows for harmonic analysis with the discrete Fourier transform," *Proc. IEEE*, vol. 66, pp. 51–83, Jan. 1978.
- [28] L. Peters, Jr., J. J. Daniels, and J. D. Young, "Ground penetrating radar as a subsurface environmental sensing tool," *Proc. IEEE*, vol. 82, pp. 1802–1822, Dec. 1994.
- [29] C.-C. Chen, M. B. Higgins, K. O'Neill, and R. Detsch, "Ultrawide-bandwidth fully-polarimetric ground penetrating radar classification of subsurface unexploded ordnance," *IEEE Geosci. Remote Sensing*, vol. 39, pp. 1221–1230, June 2001.
- [30] D. J. Daniels, *Surface Penetrating Radar*. London, U.K.: IEE Press, 1996.
- [31] C.-C. Chen, S. Nag, W. D. Burnside, J. I. Halman, K. A. Shubert, and L. Peters, Jr., "A standoff, focused-beam landmine radar," *IEEE Trans., Geosci. Remote Sensing*, vol. 38, pp. 507–514, Jan. 2000.
- [32] J. B. Rhebergen, A. P. M. Zwamborn, and D. V. Giri, "Design of an ultra-wideband ground-penetrating radar system using impulse radiating antennas," in *Proc. 2nd EUREL Intl. Conf. Detection of Abandoned Land Mines*, Edinburgh, U.K., Oct. 1998, pp. 45–49.
- [33] B. Sai and L. P. Ligthart, "Wideband short-range GPR interferometric phase processing for 3D rough surfaces with correction of antenna phase distortions," *Proc. IEEE Antennas Propagat. Soc. Int. Symp.*, vol. 3, pp. 688–691, June 2002.

- [34] W. A. van Cappellen, R. V. de Jongh, and L. P. Ligthart, "Potential of ultra-short-pulse time-domain scattering measurements," *IEEE Antennas Propagat. Mag.*, vol. 42, pp. 35–45, Aug. 2000.
- [35] J. Marti-Canales, L. P. Ligthart, and A. G. Roederer, "Performance analysis of a compact range in the time domain," *IEEE Trans. Antennas Propagat.*, vol. 50, pp. 511–516, Apr. 2002.
- [36] T. J. Cui, W. Wiesbeck, and A. Herschlein, "Electromagnetic scattering by multiple dielectric and conducting objects buried under multi-layered media, part I: Theory," *IEEE Trans. Geosci. Remote Sensing*, vol. 36, pp. 526–546, Mar. 1998.
- [37] G. W. Stroke, *An Introduction to Coherent Optics and Holography*, 2nd ed. New York: Academic, 1969.
- [38] D. C. Ghiglia and M. D. Pritt, *Two-Dimensional Phase Unwrapping, Theory, Algorithms, and Software*. New York: Wiley, 1998.



**Bin Sai** (M'02) received the B.Sc. degree from Shandong University, Jinan, China, the M.Sc. degree from Academy II of China Ministry of Aerospace Industry, Beijing, China, and the Ph.D. degree from Delft University of Technology, Delft, The Netherlands, all in electrical engineering.

In 1988, he joined the China Aero-Space Corporation, Beijing. Since April 1997, he has been a Research Scientist with the International Research Centre for Telecommunications-Transmission and Radar, Delft University of Technology. In July 2003,

he joined Enraf B.V. of the Delft Instruments Group, Delft, The Netherlands, as a Radar Specialist. His main research interests include ultra-wideband radar systems, coherent radar signal processing and imaging, nondestructive testing and precision-level gauging, and high-resolution subsurface sensing.



**Leo P. Ligthart** (M'94–SM'95–F'02) was born in Rotterdam, The Netherlands, on September 15, 1946. He received an Engineer's degree (cum laude) and a Dr.Tech. degree from Delft University of Technology, Delft, The Netherlands, in 1969 and 1985, respectively. He received Doctorates (honoris causa) from Moscow State Technical University of Civil Aviation, Moscow, Russia, in 1999, and Tomsk State University of Control Systems and Radioelectronics, Tomsk, Russia, in 2001.

Since 1992, he has held the Chair of Microwave Transmission, Radar and Remote Sensing in the Department of Information Technology and Systems, Delft University of Technology. In 1994, he became Director of Delft University's International Research Center for Telecommunications-Transmission and Radar. His principal areas of specialization include antennas and propagation, radar, and remote sensing, but he has also been active in satellite, mobile, and radio communications. He has published over 300 papers.

Dr. Ligthart is a Fellow of IEE and an Academician of the Russian Academy of Transport.